# Probing Thermal Effects in VCSELs by Experiment-Driven Multiphysics Modeling

Pierluigi Debernardi, Alberto Tibaldi, Markus Daubenschüz, Rainer Michalzik, Michele Goano, and Francesco Bertazzi

*Abstract*—**Probing the thermal effects that limit the performance of VCSELs reveals an intricate interplay between carrier transport, recombination mechanisms, thermal conduction, and optical features. An understanding of this interplay requires an accurate yet computationally efficient multiphysical approach at the microscopic level. We address this task by characterizing oxide-confined multi-mode 850 nm VCSELs over a wide temperature range, and by simulating them with VENUS, our in-house multiphysics simulator. The agreement with the experimental results in the whole explored temperature range provides physical insight into the mechanisms that determine VCSEL rollover and turn-off, and demonstrates the predictive capabilities of the model. A complete set of model parameters determined through this combined experiment-simulation approach is presented.**

*Index Terms*—**VCSELs, multiphysics simulation, drift-diffusion, electrothermal**
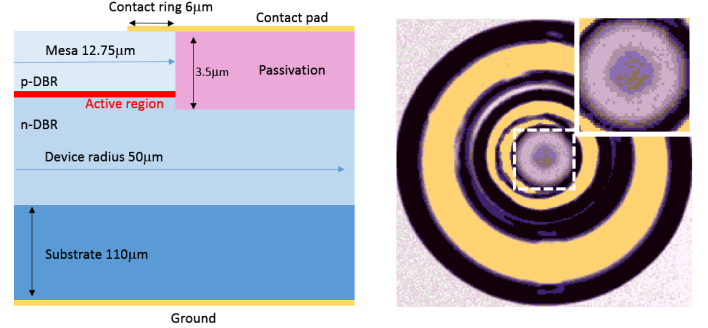


Fig. 1. Left: schematic cross-section of the device in cylindrical coordinates, providing the main geometrical sizes. Right: top image of the measured device. The metal contact is colored and the inset shows the metal ring aperture, emphasizing the central oxide aperture.

## I. INTRODUCTION

**M**ORE than 40 years after their birth, vertical-cavity surface-emitting lasers (VCSELs) are by far the preferred semiconductor light sources for sensing and data communications [1]. Nevertheless, the appetite for VCSELs is far from being satisfied, since they are enabling devices in several on-development innovations. Among their "competitors", these lasers have in fact unique features in terms of power consumption, reliability, testability, packaging costs and array-oriented manufacturability, making them the ideal light source for portable applications [2], [3]. This is why VCSELs are invading the smartphone and automotive markets, as key components in 3D cameras and LiDARs, whose potential has been just demonstrated.

Addressing the forthcoming VCSEL demand will require reliable CAD tools aimed at supporting or even replacing the extensive prototype manufacturing campaigns at the basis of their design. However, VCSEL modeling is a rather delicate task. In fact, predicting even the most basic VCSEL features such as the *LI* characteristics requires to address not only the entangled interaction of optical and electrical phenomena, but also to include all the temperature-dependent effects that rule

VCSEL performance. This is why a comprehensive VCSEL model must treat these three physical worlds and their complex interplay, as, *e.g.*, those proposed by Streiff *et al.* [4] and recently by Mehta *et al.* [5].

Due to the high interest on this topic, some simulation codes are commercially available: previous versions of ISE TCAD [6] featured the model described proposed by Streiff, but at present it is no longer supported nor documented [7]. Sentaurus could be potentially coupled to LaserMOD [8] from Synopsys RSoft, whose optical solver is scalar. Another commercial modeling suite that can be used for VCSEL simulation is PICS3D [9] from Crosslight Software.

Resulting from the authors' experience in optical and electrical modeling, the in-house simulator VENUS (Vcsel Electro-optho-thermal NUmerical Simulator) aims to advance the field of comprehensive VCSEL modeling. We in fact believe that only by a 100% mastering of an in-house simulator it is possible to make all the needed tests, and to include all the necessary ingredients, or to modify them, in such a way to achieve a better understanding and an improved match with real device performance. The model and some preliminary applications to previous experimental results is already fully described in [10]. Instead of repeting the theoretical foundations, in this paper we focus on the measurements recently performed in Ulm, to deepen the knowledge of VCSEL thermal features. Moreover, these experimental results enable the investigation and calibration of the major thermal dependencies via extensive parametric numerical comparisons.

## II. DEVICE STRUCTURE AND EXPERIMENTAL RESULTS

We investigate an oxide-confined AlGaAs VCSEL, whose cross-section is schematically depicted in Fig. 1, together with
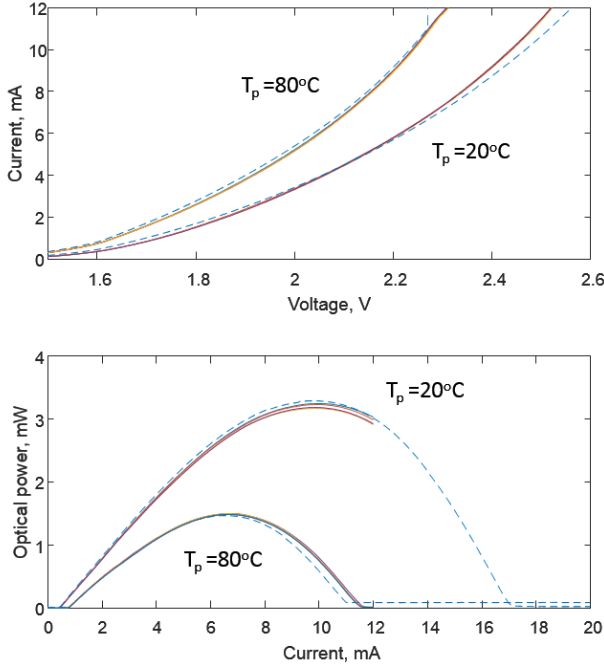
Fig. 2. *IV* (top) and *LI* (bottom) characteristics for two ambient temperatures of 4 μm oxide aperture VCSELs. The four colors refer to four nominally identical devices, while the dashed line correspond to one of them, remeasured at a later time on an extended current span.
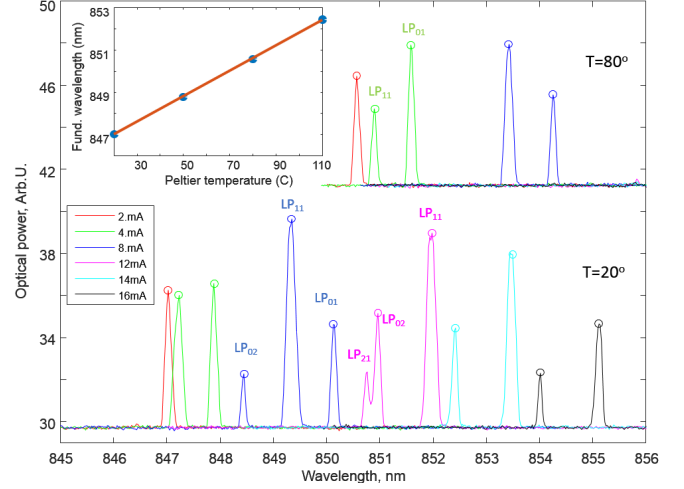


Fig. 3. Optical spectra for two different ambient temperatures. The higher temperature has been shifted by 12 dB to allow for a clearer representation of the spectra. The different colors refer to different currents. The inset shows the fundamental mode wavelength at 2 mA vs. temperature (blue dots) and their linear fit.

a real image taken from the top of one of the measured devices. It features the following main characteristics: the $1\lambda$-cavity embeds three 8 nm GaAs quantum wells (QWs), placed at the maximum of the optical standing wave. The 30 nm oxide layer is placed in the first of the 21 pairs of the $p$-DBR outcoupling mirror. The corresponding oxide aperture at the device axis provides both current and optical confinements; the bottom DBR includes 37 pairs. Both mirrors are subjected to composition [11] and doping gradings to improve the electrical conduction and, at the same time, to keep the free-carrier absorption losses at a minimum. Other details on the investigated structure will be provided in Section III, when discussing how they are included in VENUS.

Several VCSELs from the same wafer have been processed in arrays, featuring columns with the same nominal oxide aperture and rows with different oxide apertures, ranging from 1 to 10 μm. Since in this paper the main focus is to investigate thermal features, we select just one 4 μm oxide aperture device, which supports up to four transverse modes in its operation range. In fact, characterizing transverse-mode competition is important, since it allows to access the in-plane carrier transport features of the QWs.

An essential feature of our investigation is the possibility to vary the device temperature independently from the intrinsic operation heating. To this aim, the devices are mounted a temperature-controlled wafer chuck and all the experimental results (*LIV* and spectra at selected currents) have been recorded at 20, 50, 80, and 110 °C.

Several devices with nominally the same size have been measured, aiming to quantify their reproducibility. This is shown in Fig. 2, where the four *VI* and *LI* characteristics

are reported for two ambient temperatures ($T_A$). Those experimental results were recorder earlier, in relation to former investigations [12], and in November 2018 performed again just for one device to meet several requirements related to the present investigation. Essentially, an extended current range was applied to explore the whole operation range, from threshold to turn-off, and the spectra were recorded at more currents. The extended current range can be seen in the *LIV* curves by the dashed lines, which are the experimental data compared with VENUS results presented in what follows. The comparison between the two experimental set of results is interesting in itself, because it allows to have an idea of the uncertainties of the measurement setup. They are bigger than device reproducibility on chip. Therefore the error on the experimental quantities is of few percents, and a maximum tolerance in the optical measurement setup calibration is estimated in ±10%.

Fig. 3 reports the optical spectra for two ambient temperatures and different bias currents. Since all the measurements have been performed disregarding polarization (no polarizer was included in the set-up), no polarization features will be considered in this paper. For this reason also VELM, our in-house optical solver [13], [14], has been run in its scalar version, which is faster and does not imply any relevant loss of accuracy for this kind of structure. Therefore the modes are referred by using the common LP notation: $LP_{01}$ for the fundamental, Gaussian-like mode, $LP_{02}$ for the second radial mode with no azimuthal variations, $LP_{11}$ for the first-order mode, etc. In the figure, some of the spectral peaks are labeled, to guide the reader. As a reference, the radial profiles of the first three transverse modes are also shown in Fig. 6.

It is to be remarked that VENUS is fully equipped and ready to deal with vectorial fields and polarization features, which could be needed in the case the VCSEL includes a grating [15]. In fact, its optical engine can efficiently include any kind of anisotropy, either induced by the material (electro-

or elasto-optic effect [16], [17], [18]) or by the geometry (non-circular shapes [19] and, most importantly, gratings [20] or high-contrast-gratings [21], [22], [23], [24]). While VELM can treat any kind of transverse geometry, VENUS is still limited to circular symmetries for what concerns the device sections that have an impact on the electrical transport, *i.e.*, the metal $p$-contact and the oxide aperture. Since almost all devices are based on a metal ring and a circular mesa, this does not constitute a too severe limit. In fact, as can be seen in Fig. 1, the oxide is quite circular, even if few faint signs of a rhomboidal shape can still be noticed [25]. However, from the spectra, there is no signature of such small non-circularity, at least within the spectral resolution used here.

From the experimental results it can be be seen that, at both temperatures, only the fundamental LP$_{01}$ mode is present at 2 mA. At 110 °C (not shown) single-mode operation is maintained through the whole bias range. On the contrary, at room temperature the richest transverse mode behavior occurs. At increasing bias current the second mode soon appears, and, at 8 mA, also the LP$_{02}$ mode shows up. Since both LP$_{01}$ and LP$_{02}$ modes have their maxima on the VCSEL axis, they are competitors from the spatial-hole-burning perspective. Therefore, the rise of the LP$_{02}$ mode causes eventually the fundamental-mode turn-off. In fact, at 12 mA LP$_{01}$ is off and the leftmost double peak corresponds to LP$_{02}$ and LP$_{21}$ modes, which are very close in wavelength, as also shown by VELM results.

Such optical spectra are fundamental to grasp the thermal characteristics of VCSELs. In fact, the wavelength dependence on temperature is the only simple "thermometer" available, even if it provides an indirect and optically weighted information [26].

The refractive index can be assumed to vary linearly with temperature [27], [28] according to the standard formula

$$n(T) = n(T = 300 \, \text{K}) + \frac{dn}{dT}(T - 300 \, \text{K}). \quad (1)$$

The coefficient amounts to units in $10^{-4} \text{K}^{-1}$ and is directly determined from the measurements in the following way. Using the first available spectra at 2 mA, where the temperature profiles are still minor (always less than 20 K maximum increases), the fundamental mode position is plotted vs. ambient temperature and fitted with a line (inset of Fig. 3). From the resulting wavelength slope $d\lambda/dT$ one gets

$$\frac{dn}{dT} = \frac{\bar{n}}{\lambda} \frac{d\lambda}{dT}, \quad (2)$$

where $\bar{n} = 3.25$ is an effective VCSEL refractive index resulting from the refractive index stack weighed by the longitudinal electric field intensity standing wave. At $\lambda = 850$nm the refractive index thermal coefficient amounts to $2.3 \times 10^{-4} \text{K}^{-1}$ and exactly matches the value of Table III in [28]. This value will be used in all the simulations presented in this paper.

## III. VENUS SIMULATION DETAILS

In this section we describe how the actual device is described in VENUS, and some of the corresponding parameters. All the structure layers are listed in a text file, containing
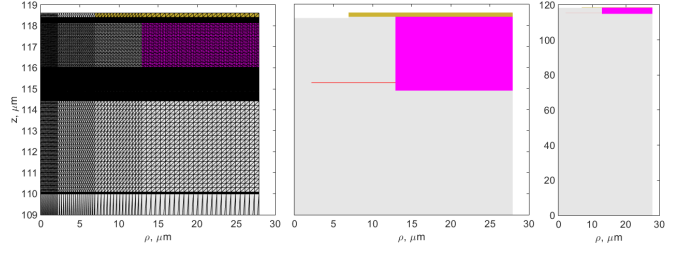


Fig. 4. Device cross-section, limited to the drift-diffusion computational window, illustrating the main transverse features of the device under analysis. Left: mesh of the electrical solver, longitudinally zoomed onto the VCSEL section. Center: same as left, without showing the mesh (see text for the description of the different regions). Right: the whole simulated geometry, including the $110 \, \mu$m thick substrate.

all the position-dependent optical, thermal and electrical parameters. The highest complexity resides in the longitudinal variations. Each layer is represented by a line of the text file, where linear parameter gradings can be specified by providing their value at the two extremes: semiconductor composition (Al content in this case) and doping profile. Each layer may have radial refractive index variation, such as the oxide region. Any parameter in this structure can be tagged as "variable", so that VENUS can parametrically modify it. This feature is important in the parameter calibration stage. Electrical (*e.g.*, mesa, equivalent DBR sections and passivation) and thermal regions, which do not require a degree of detail as the optical part, are treated in a separate section of the file.

Since the VCSEL is grown on an $n$-doped GaAs substrate, later thinned to $110 \, \mu$m and fully included in the simulation, the mesh is longitudinally denser in the VCSEL volume. This can be appreciated in Fig. 4, where just a portion of the substrate domain is visible. A coarser $3 \, \mu$m longitudinal discretization is applied in the substrate, where the electrical quantities vary slowly. In the present simulations most of the DBRs are substituted with an effective medium, maintaining the complete structure for just few of the pairs adjacent to the cavity (4 $n$- and 6 $p$-pairs) . Such an approach, first proposed in [4] and investigated in detail in [29], has been calibrated by comparisons with the full structure, where all the DBR details are included. Simplifying the DBRs allows to relax the grid, leading nevertheless to 27496 mesh nodes (76 radial and 365 longitudinal points). This corresponds to a number of equations roughly threefold compared to that of the nodes, related to the three unknowns of the drift-diffusion solver: electric field, electron and hole densities in every point of the grid. The difference in the longitudinal spatial sampling can be clearly appreciated in Fig. 4, where it is denser in correspondence of the cavity and below the metal ring. Moreover, the drift-diffusion equations are solved only in correspondence of the semiconductor regions. In the passivation and oxide regions the current continuity equations are disabled, enforcing insulating boundary conditions. Only Poisson's equation, which is defined on the same electrical grid, is solved on the whole mesh.

It has to be remarked that only the drift-diffusion solver relies on a spatial discretization, whereas both thermal and
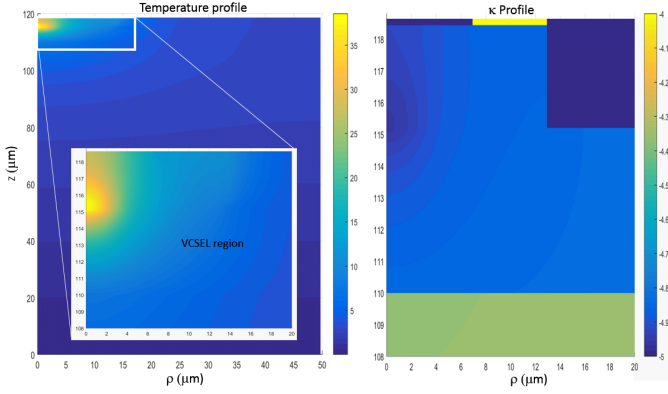
Fig. 5. Left: temperature map, with a zoom on the VCSEL region (inset). Right: corresponding nonlinear thermal conductivity map zoomed on the same VCSEL region. Ambient temperature is $20\,^{\circ}$C, operation current $6.5\,$mA.
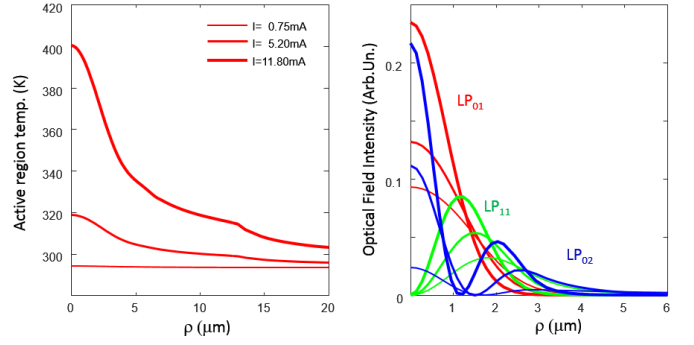


Fig. 6. Left: temperature radial profile at the MQW section for three bias currents coded by line thickness. Right: the corresponding transverse optical mode intensity profiles.

optical solvers are based on modal expansions and in a full 3D environment [30]. In other models, where the thermal and optical problems are solved on different meshes, it is necessary to remap the different grids one into the other. VENUS is free from this issue; both optical and thermal solvers use the drift-diffusion inputs on their original grid to compute the projections on their modal basis. This reduces the multiphysics couplings to the simple evaluations of the optical and thermal quantities on the drift-diffusion mesh points.

The VCSEL features a mesa of nearly $13\,\mu$m radius (see Fig. 1 and Fig. 4, center) to apply the oxidation of the exposed AlAs layer. After the oxidation process, a passivation layer (in magenta) is deposited to insulate the mesa sides and reduce the parasitic capacitance. The current is then injected through the $6\,\mu$m wide metal ring deposited on the top GaAs layer, where an ohmic contact is obtained by a $p^{++}$-metal junction. Notice that the electrical domain comprises the whole mesa and extends more than twice in the radial direction (see Fig. 4). This domain was determined by increasing its boundary until the solutions did not change any longer.

### A. Thermal solver

The thermal profile rules the VCSEL operation. Since in this paper we focus on thermal phenomena, it is useful to provide additional details regarding the thermal solver and the related issues. The thermal diffusion equation to be solved is in the form

$$\nabla \cdot (\kappa \nabla T) = -Q_{\text{tot}}, \qquad (3)$$

where $\kappa$ is the thermal conductivity and $T$ is the temperature increase relative to the ambient temperature. In a VCSEL it is possible to identify several regions characterized by different thermal behaviors, i.e., different $\kappa$'s: the substrate, the passivation, the DBRs, the QWs, and the contacts. For the values used in this paper, refer to [10] with the only difference that for the most important regions (the DBRs and the cavity, where the heat source is maximum), we adopted $\kappa_t = 15$ W/m/K, equal for both DBRs and cavity. This value is an average of all the graded composite layers and the lowest conductivity value of about 10 W/m/K dominates compared to the higher values of the two binary alloys [31].

An anisotropy factor of 0.8 is used to account for the reduced thermal conductivity in the longitudinal direction $\kappa_z$ [32], [33].

While moving from the ground towards the $n$-DBR the temperature increase is almost linear, in the active part much steeper variations can be observed. Such behaviors are consequences of the diverse (effective) thermal conductivities, but also of the heat sources computed from the electrical simulation variables [10].

In most simulators, the thermal problem is usually addressed by the finite element method (FEM), which consists of an extensive spatial discretization of the whole VCSEL domain, possibly including the substrate, aimed at defining a set of linearly-varying basis functions, one for each mesh node. According to the widely-used Galërkin formulation of the method of the weighted residuals, these basis functions are used to expand the unknown (temperature profile) and to project the heat equation. This allows to transform the partial differential equation into a linear system, whose known term is obtained by evaluating the heat sources in the mesh nodes. This approach is by far the favorite in the modeling community. In fact, FEM is very flexible in the description of geometrical and physical (e.g. thermal conductivities) properties. Moreover, it can be implemented with very moderate effort thanks to the plethora of available libraries. Finally, the typical sparse pattern of the system matrix enables fast solution. On the other hand, FEM exhibits poor convergence properties under mesh refinements, leading to the requirement of a huge number of mesh nodes to achieve good accuracy.

The VCSEL thermal problem does not require great flexibility of the geometry and physical parameters, since the thermal conductivities can be assumed piecewise-constant on cylindrical (or rectangular, in 2D) domains. Still, an efficient numerical scheme should account for the different temperature variation regimes to keep the number of degrees of freedom at a minimum. Therefore, in order to guarantee reasonable to enhance the FEM convergence properties, the thermal solver adopted in this work is based on the mortar element method (MEM) [34], [35]. In MEM, the mathematical formulation aimed at reducing the differential equation to a linear system is similar as in FEM, based on the Galërkin scheme. The major difference lies in the set of basis functions. In fact, in MEM the domain is decomposed in few subdomains, corresponding

to the number of regions with different physical properties. Then, a set of high-order basis functions is defined for each subdomain. This is usually the double/triple tensor product of Legendre or Chebyshev polynomials for 2D/3D problems. The boundary conditions of the thermal problem (fixed temperature at the ground contact and heat flux continuous at the interfaces between different materials and zero above the $p$-contact), are enforced in weak form by specializing these local high-order functions by the mortar method. According to the mortar method, the boundary condition is projected (just like the differential equation) on test functions defined at the interfaces where it must be enforced, leading to homogeneous linear systems. The solutions of these systems, which can be obtained by the singular value decomposition, can be used as change of basis from the initial, non-specialized functions to the final functions to be adopted in the problem discretization. Several details about the synthesis of the basis functions can be found in [34], [36]. Most of the elements of the system matrix can be obtained by analytic integrals, so filling the system matrix is at zero computational cost. Moreover, they depend only on the geometry and are pre-computed just one time. The only integrals requiring numerical computations are involved in the known-term evaluation, which is performed by projecting the heat sources on the test functions. The entire VCSEL thermal problem can be discretized with approximately 50 basis functions. Even though the corresponding system matrix is strongly dense, the quasi-exponential convergence MEM features typical of spectral methods [37] guarantee a much higher convergence than in standard FEMs, with comparable memory occupation and CPU usage.

All the above discussion holds true in case of $\kappa$ profiles independent from temperature. However, this is not the case and, as it will be shown, plays an important role in VCSEL operation. The dependence of the thermal conductivity from temperature is usually assumed to follow [38]

$$\kappa = \kappa_{300\,\mathrm{K}} \left( \frac{T}{300\,\mathrm{K}} \right)^{-\beta_T}. \tag{4}$$

It has been found that it is not sufficient to adopt the temperature profile of the previous voltage point to evaluate the actual thermal conductivity profile, especially if the voltage sampling is kept moderate, so as to speed up parametric campaigns. Therefore, we resorted to a more refined approach, seeking for the self-consistency of the thermal profile at each working point. This is achieved by an iterative procedure, where the $\kappa$ profile is updated until the maximum relative temperature deviation compared to the previous iteration falls below a specified value ($10^{-3}$ in the present case). Three to four iterations reach the required precision, and the whole thermal solver takes just ten seconds per bias point.

As an example, in Fig. 5 we show a typical thermal profile of our device. The need of spatial dependent basis-function resolution clearly appears, since in the substrate the thermal dependence is nearly linear, while it is strongly peaked in the active region. From the figure one can appreciate the different thermal conductivity regions, where the temperature profiles show a derivative change caused by the continuity of the heat flux. At right, we provide the corresponding nonlinear profile of the thermal conductivity.

To complement the previous result, Fig. 6 reports the transverse temperature profiles at different operation currents. In this figure, the derivative change of the profile can be seen more clearly at the mesa–passivation interface. It is interesting to show, at least once, the corresponding optical field intensity profiles, reported at right. Here one can appreciate the strong thermal lensing effects related to the temperature profiles shown at the left. The fields squeeze to the device axis quite impressive. This indicates that refractive index variations are very important in a VCSEL optical simulation. In fact, apart for the weak transverse index guiding at the oxidation section, the transverse index profile is essentially "flat" from the optical field perspective. Therefore, even small refractive index, real and imaginary part (losses), spatial profiles induced by temperature (thermal lensing) and free carriers (index reduction and loss increase) have a strong impact on the optical problem. They are therefore updated at every voltage step, when calling VELM. The QW refractive index reduction due to increased carrier densities is self-consistently introduced, as it is the real part of the susceptibility from which the gain is computed. It is responsible for the small modal wavelength decrease below threshold reported in the results which follows.

## IV. INVESTIGATION AND CALIBRATION OF THE MAJOR THERMAL DEPENDENCIES

Most of the parameters involved in the physics of a VCSEL depend on temperature and this plays an important role because the temperature range in a VCSEL is wide. In fact, the power rollover typically occurs between 100 and 150 °C above room temperature. Moreover, considering to start from a higher ambient temperature, like in our experiments, or in the field, when devices are housed in hot environment (cases, motors, etc.), the temperature range where the parameter dependence is to be known reaches 200 °C, i.e. from 300 to 500 K.

The aim of this paper is to identify and investigate the most important of the thermally dependent parameters:

1) gain, modal spontaneous emission (MSE), spontaneous emission (SE)
2) bandgap, which impacts on both the optical gain and electrical features,
3) mobility
4) thermally dependent free-carrier absorption
5) recombinations, especially Auger

Thermally dependent refractive index variation and thermal conductivity do not appear in the above list because we already discussed them before.

After an extensive parameter tuning campaign we achieved a satisfactory agreement between model and experiment over the whole range of temperature and bias currents.

It is useful to present in Table I the investigated parameters and their numerical values after the optimization campaign. For those not listed here, refer to Table I in [10]. The table features: physical effect, parameters that phenomenologically models it, with the notation used in the corresponding equations, three columns (O, E, T) for the three Optical, Electrical

TABLE I
ELECTRICAL (E), OPTICAL (O) AND THERMAL (T) PARAMETERS OF
$Al_xGa_{1-x}As$ (UNITS OMITTED).

| Effect | Par | O | E | T | Value |
|--------|-----|---|---|---|-------|
| Mob. (6) | $N_X \cdot 10^{-18}$ | | + | | $(0.15 - 0.011T_A)$ |
| Mob. (6) | $\beta_{n,p}$ | | + | | 0.4 |
| FCA (7) | $f_\alpha$ | + | - | - | $(2.6 - 0.019T_A)$ |
| FCA (7) | $\beta_\alpha$ | + | - | - | 2.5 |
| Auger (8) | $C_N$ | +S | +S | - | $0.5 \cdot 10^{-30}$ |
| Auger (8) | $\beta_{Aug}$ | +S | +S | - | 1 |
| T. Cond. (4) | $\kappa_{DBR}$ | + | + | + | 15 |
| T. Cond. (4) | $\beta_T$ | + | + | + | 1.3 |
| Diffusion | $f_{Diff}$ | + | + | | 0.4 |
| Index (1) | $dn/dT$ | + | | | $2.3 \cdot 10^{-4}$ |



Fig. 7. VENUS output chart (see text), varying the driving source DC: 1 (green), 0.6 (red), 0.1 (blue).

and Thermal problems, to indicate the impact of a given parameter on the corresponding aspects. The notation + (-) implies a strong (minor) impact, as will be shown by the following parametric variations. The notation +S means the impact is strong only in gain saturation regimes, which in the present case means high operation temperature. The units of measure are not reported for lack of space; for them, refer to Table I in [10]. In two cases, the parameter depends on the ambient temperature (see discussion related to Fig.s 9 and 10). In that case, $T_A$ is the ambient temperature in Celsius and dimensionless. The factor $f_{Diff}$ is defined as: $D_{nQW} = f_{Diff} D_{nBulk}$, that is a factor that impacts on the nominal diffusion coefficient for the corresponding bulk material.

In what follows we provide a detailed discussion of those parameters, and their thermal dependence. For that purpose, we deploy "reduced VENUS output charts". There, only the observable quantities are presented next to the measured data. Since such charts are extensively used in the rest of the paper, it is useful to present here one of them in detail. To that purpose, we exploit one of the 60 parameters that VENUS can handle currently, beyond the structural ones previously mentioned.

VENUS is a steady state solver, so also temperature is treated in CW (continuous wave). In early VCSEL design stages, heating problems are/were circumvented by pulsed operation regime. This can be easily mimicked in VENUS by applying a coefficient to the computed thermal-increase profile, which is related to the duty cycle (DC) of the pulsed driving source.

In Fig. 7 the VENUS chart presents the dependence of the "observable outputs" for different DCs. The chart presents four plots vs. driving current:

- top-left: *IV*
- top-right: *LI*
- bottom-left: differential resistance
- bottom-right: fundamental mode wavelength

In every plot, the dots represent the experimental results, the lines the simulations; their colors correspond to different parameter values. In this section, results are always presented in pairs, corresponding the two extremes of the measured temperature range (20-110 °C). Room temperature is repre-
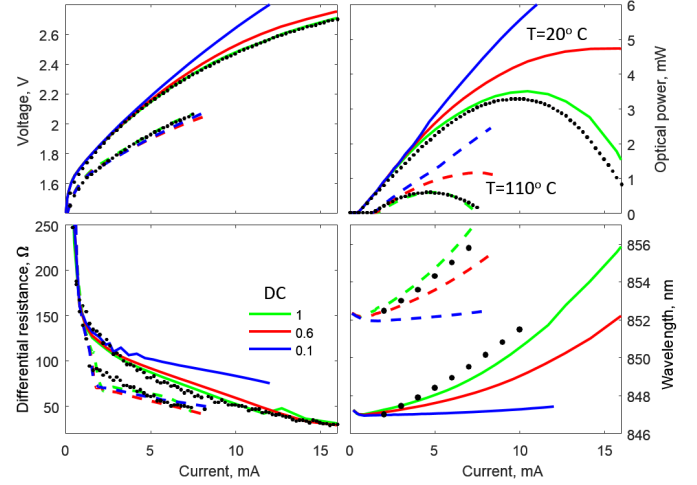
sented by continuous lines, which allows also to identify the corresponding experimental curve, by its proximity with the computed results. It is worth to point out that the differential resistance is a very sensitive parameter, emphasizing small numerical errors, invisible in the *IV* plots. The oscillations in the computed differential resistance are usually of few ohm, and typically occur where a new optical mode start lasing.

Regarding the specific parametric investigation of Fig. 7, this is a clear proof that thermal effects rule VCSEL operation. In fact, without thermal effects, optical power increases linearly with current and no rollover occurs, since all the quantities stay blocked at the threshold value. At DC=0.1 it nearly remains just the fixed ambient temperature, which shows a big impact on all the features reported in the chart. In particular, at high temperature the voltage is lower, as the differential resistance, and the optical power very reduced. The 0.45 mA threshold current increases to 1.35 mA (three times), the maximum power reduces from 3.3 mW to 0.6 mW and, correspondingly, the wavelength shifts by about 5.5 nm. The numerical results in CW (green curves), fit well the experiments.

In what follows we discuss and provide detailed information on how such and agreement can be achieved.

### A. QW gain and bandgap thermal dependence

In the list provided at the beginning of this section, gain stands in the first place. In fact, it is one of the four blocks into which VENUS is subdivided (see Fig.1 of [10]). Gain is literally the "engine" of the VCSEL and some details of the VENUS gain model can be found in [10]. Here it suffices to recall that gain computation is tackled via look-up tables, which are computed *a priori* just once and re-used unless the QW size or barrier are changed. Such tables are then interpolated at the needed variable values dictated by the temperature (T), optical ($\lambda$) and drift-diffusion ($n, p$) solvers.

In Fig. 8 we provide two cuts of the computed 4D matrices of the gain and modal spontaneous emission. The four matrix independent variables are: electron and hole densities, temperature, and wavelength. The total spontaneous emission,
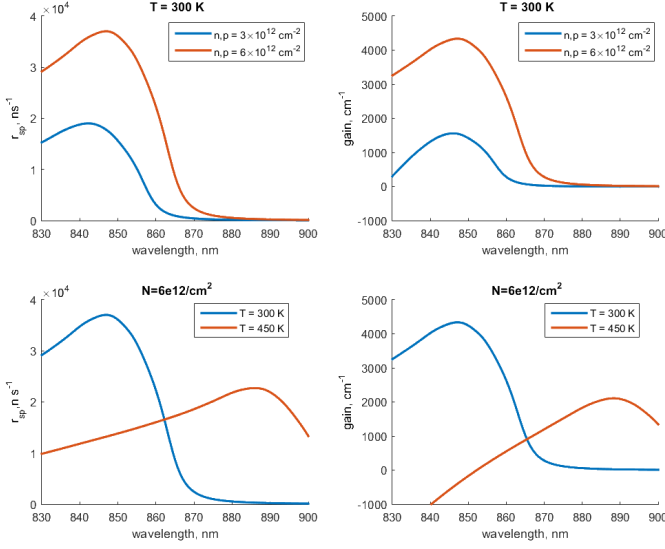
Fig. 8. Modal spontaneous emission (left) and gain (right) spectra at room temperature for two carrier concentrations (top), and for two temperatures at a fixed carrier concentration (bottom).
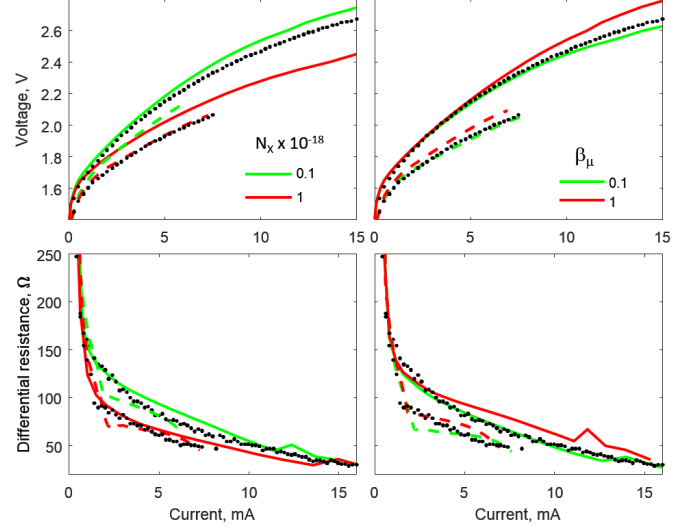


Fig. 9. VENUS electrical output chart (see text, only electrical characteristics are shown), varying the Hilsum formula parameters (6). Left: varying $N_X$. Right: varying $\beta_\mu$

in turn, does not depend on wavelength, so it is just a 3D variable; in fact it can be regarded as the integral over the whole spectrum of the modal spontaneous emission. It is to be remarked that both MSE and SE (modal - spontaneous emission) are computed similarly to gain. This leads to the elimination of both the $Bnp$ recombination term and the so-called "$\beta$-parameter", which is frequently used as a measure of the fraction of the total spontaneous emission into the lasing mode (written as $\beta R_{sp}$). VENUS does not use these approximated approaches, but instead includes self-consistently the variation of spontaneous emission with carriers, temperature, and wavelength (the latter only for MSE).

The most striking effect in the QW optical response, in both gain and MSE, is the wavelength red-shift of the gain spectrum with temperature. The bandgap thermal dependence is modeled by the standard Varshni model [39] as

$$E_g = E_{g,0} - \alpha_g \frac{T^2}{\beta_g + T}. \tag{5}$$

This effect is very important and impacts on both optical (gain and spontaneous recombination) and electrical (drift-diffusion) features. It is also worth to recall that, starting from similar expressions for the other two electron valleys bandgaps, the electron densities of states is evaluated in a many-valley perspective [29], which then implies an additional temperature dependence in the model.

### B. Mobility

Keeping following our list, we investigate now the mobility, the most relevant parameter for the electrical problem. Since, to some extent, it does not have a strong impact on the LI features, we discuss it and its thermal dependence just on the electrical characteristics. It must be beared in mind that mobility is a simplified description which implies small internal electric fields; it seems however a valid approach in

a VCSEL and is therefore applied in VENUS. Mobility is far from being known with great accuracy, including the fact that the actual doping profile can deviate from the targeted one. In VENUS, mobility is described phenomenologically by the modified Hilsum formula [40]

$$\mu_{n/p} = \frac{\mu_{n/p,\text{int}}}{1 + \left(\frac{N_A + N_D}{N_X}\right)^{0.35}} \left(\frac{T}{300\,\text{K}}\right)^{-\beta_{n/p}}, \tag{6}$$

where $\mu_{n/p,\text{int}}$ indicates the alloy-dependent mobility of the intrinsic material, and $N_D$ and $N_A$ are the donor and acceptor doping concentrations respectively. Usually mobility is assumed to follow a temperature power law, where, however, the exponent $\beta_{\mu,n/p}$ are not well known. In this work both $\beta_\mu$ and $N_X$ are treated as fitting parameters and their effect is investigated in Fig. 9. There, for lack of space, only the electrical part of VENUS charts is reported, which allows us to show in the same figure the effect of both parameters.

The dependence of mobility on doping concentrations is a major effect, strictly necessary to have acceptable comparisons with experimental results. In this work we use a modified Hilsum expression, where the power in the denominator is 0.35 instead of 0.5. The different exponent was determined by fitting Hall measurements of mobility at room temperature (see Acknowledgement Section), together with a value of $N_X = 10^{17}\,\text{cm}^{-3}$.

The effect of varying this phenomenological parameters is illustrated in Fig. 9. It can be seen that at room temperature the electrical features are quite satisfactory, and we find a best fit of the IV curves for $N_X = 1.5 10^{17}\,\text{cm}^{-3}$, which is very close to the previous results based on *ad-hoc* bulk samples and direct fits of the measured Hall mobilities.

Instead, at $110\,^\circ\text{C}$ (dashed green curve) the deviation is quite large. A good fit occurs instead for $N_X = 10^{18}\,\text{cm}^{-3}$; this ask for a temperature dependence of $N_X$, which somehow compensates/counteracts the mobility decrease implied by the
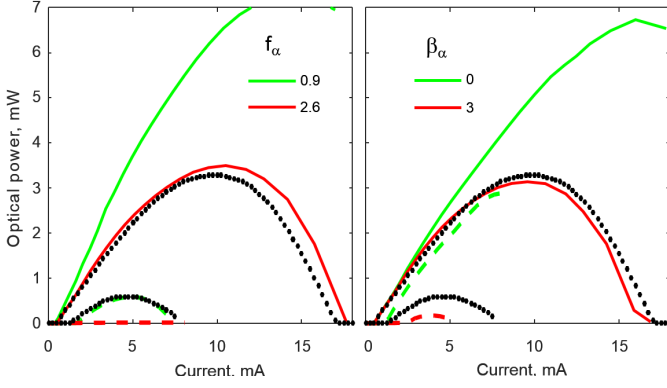
Fig. 10. VENUS optical output chart (see text, only *LI* characteristics are shown). Left: varying the absorption loss factor $f_\alpha$. Right: varying $\beta_\alpha$.



Fig. 11. VENUS output chart for different Auger parameters (see eq. 8). Top: Auger coefficient $C_n$ is varied (units of $10^{-30}$ cm$^6$/s). Bottom: Auger exponent $\beta_{\mathrm{Aug}}$ varies.

power law. The value of $N_X$ is therefore made dependent on the ambient temperature with a linear fit between the two value used in Fig. 9. In the right part of the figure, this dependence is applied and the power exponent varied to a lower and higher value compared to the adopted one. As it will be seen also for other parameters, their effect is amplified by the saturation condition at high temperature. At room temperature results are not affected significantly, while at high temperature the effects reported in the two colums are quite similar. We selected average values (0.5 and 1 respectively), only based on the high temperature performance. This well illustrate the importance of having the temperature as a degree of freedom in a parametric fit campaign.

## C. Free-carrier absorption model

Moving now to the optical performance, we discovered in the framework of this investigation that free-carrier absorption (FCA) plays a crucial role, both on threshold and *LI* curves. We first modeled such losses by applying the Drude formula, which is based on the "free-electron" oscillator model [41], and included intraband absorption for electrons [42]. However, both models summed up provide absorption losses of about one order of magnitude lower than the ones observed experimentally. Probably for this reason, in the literature more simple and phenomenological formulae are used. The dependence on free carriers is linear as in the Drude formula, but the coefficient is phenomenological. It reads as [43, p. 175]

$$\alpha = f_\alpha \left( \alpha_e \frac{N}{10^{18}\mathrm{cm}^{-3}} + \alpha_p \frac{P}{10^{18}\mathrm{cm}^{-3}} \right) \left( \frac{T}{300\,\mathrm{K}} \right)^{\beta_\alpha}, \quad (7)$$

where different coefficients pairs $\alpha_e / \alpha_p$ have been proposed in the literature, *e.g.*, 3 / 7, or 5 / 11. In this work we adopt the first pair (3 / 7), but introduce a fitting factor $f_\alpha$, which is parametrically varied in Fig. 10 (left).

Here the effect is dramatic and induces to postulate a temperature dependence also for it, as for $N_X$ of the Hilsum model. In fact, we could not find any "leverage" which compensates for so large differences between "offer" (available gain) and "demand" (absorption losses). The only possible cause that could explain such an unbalance is optical gain. In the future we would like to measure the actual gain
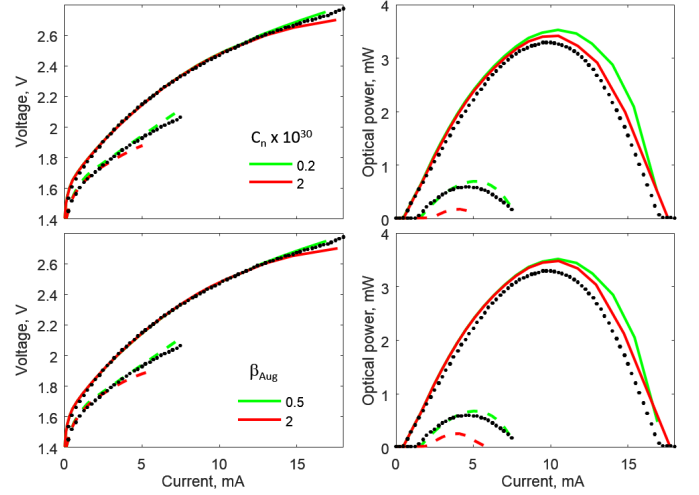
in our samples and compare it with our model. Numerical comparisons with other gain solvers already succeeded, but improvements are possible, such as including the thermal and carrier dependence of intraband scattering. Several approaches proposed in the literature, spanning from the classic Lorentzian [44] to more sophisticated models including carrier–carrier effects [45], have been pondered and we opted in the end for a model proposed by Tomita, which includes non-Markovian effects [46]. Still, the effect of intraband scattering is at present assumed constant, as also the different ingredients that concur in the standard evaluation of carrier bandgap renormalization [47]. The above effects could lead to some deviation compared to the actual gain/MSE/SE, but, as we believe, not to the extent that we observe here. In fact, using the standard "absorption rule" ($f_\alpha = 1$), at room temperature the threshold is quite well reproduced, but not the optical power slope, which is given by the output mirror losses referred to the total losses. As one can see, the influence of the high $p$-doping absorption is fully comparable with the mirror radiation losses, which are the "good" losses that convey the photons out of the cavity. Instead, the absorption losses not only consume photons inside the device, but convert them to heat, contributing to the device rollover.

If $f_\alpha = 2.6$ nicely fits the experimental optical power slope, it completely prevents laser action at 110 °C, where a good fit is achieved by $f_\alpha = 0.9$. By proceeding as for $N_X$, we use therefore a linear interpolation of $f_\alpha$ on the ambient temperature (see Table I).

Moreover, in (7) a temperature dependence of the absorption losses is also introduced with the same simple temperature power form as for other quantities discussed in this paper. On the right of Fig. 10 the effect of this parameter is investigated. Its strong impact is illustrated on the wide exponent explored range. The higher value is close to the adopted one (2.5). Disregarding this factor, would produce almost no variation on the low temperature threshold, but a strong variation of the rollover power. All is more dramatic at high temperature,
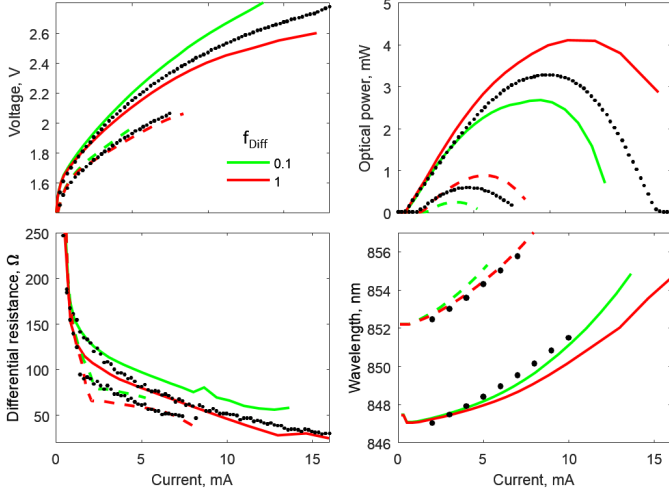
Fig. 12. VENUS output chart (see text). The electron diffusion coefficient in the QWs is varied by the factor $f_{\mathrm{Diff}}$ indicated in the legend.



Fig. 13. Comparison of the modally resolved optical powers for two values of the QW electron diffusion factor $f_{\mathrm{Diff}}$ at 20 °C. The colors correspond to different transverse mode, the different lines to: open circles, experimental results; continuous lines, $f_{\mathrm{Diff}}$=0.1; dashed lines, $f_{\mathrm{Diff}}$=1. The stars identify the fundamental-to-first-order mode crossing current points: 2.2, 4.3 (experimental) and 5.4 mA.

where the impact is huge on both threshold and output optical power.

### D. Auger thermal dependence

The last analyzed phenomenon to which frequently the power rollover is attributed, is Auger recombination. Due to the high carrier densities typical in semiconductor light sources, Auger coefficients are still a topical research subject from both theoretical [48], [49], [50], [51] and experimental [52] perspectives. Even though GaAs is a quite established material system, the literature reports a broad range of Auger coefficients [53]. Such coefficients has been suggested to feature an exponential temperature dependence [54]; for this reason, in this work we adopt this dependence

$$C_{n/p} = C_{n/p}(300\mathrm{K})e^{\frac{T-300\,\mathrm{K}}{100\,\mathrm{K}}\beta_{\mathrm{Aug}}}, \qquad (8)$$

which, written in the above form, for values of $\beta_{\mathrm{Aug}}$ around unity provides nearly one order of magnitude increase of the Auger coefficient in the range 300 to 500 K [55]. Both $\beta_{\mathrm{Aug}}$ and $C_{n/p}(300\mathrm{K})$ are varied around typical values, because, especially for QWs, Auger coefficients and their temperature variations are not well known.

The effect of varying such parameters is shown in Fig. 11. As it can be noticed, there is an impact on both electrical and optical characteristics. However, it is quite interesting to remark that the effect is minor for operation at room temperature, but it becomes very important for extreme conditions, close to gain saturation, as at 110 °C, or in particular designs, such as surface-relief VCSELs [10].

### E. Electron QW diffusion coefficient

The parameter that has a strong impact on both electrical and optical performance is the QW diffusion coefficient. In fact it governs transverse mode competition via spatial hole-burning, which distributes gain differently to each transverse mode at increasing injection. The spatial hole is dug according to the modal field intensity profiles at the longitudinal QW
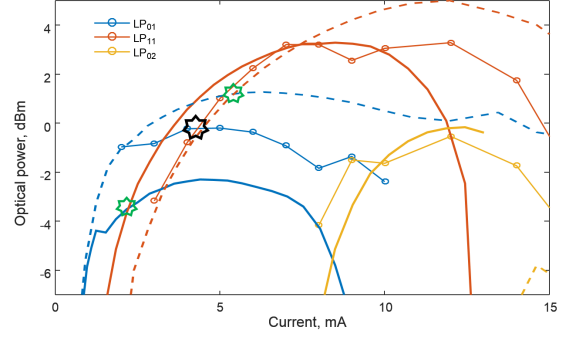
positions. The depth and final shape of such a spatial hole in the gain profile depends on the carrier diffusion and is different for electrons and holes, because of their very different diffusion coefficient. To investigate the effects of the diffusion coefficient, in Fig. 12 we strongly vary it. Its effects to all features are strong, disregarding the temperature. Lower values block carriers, with direct impact on the optical features. Carrier mobilities have been investigated and characterized in depth for bulk GaAs [38], [55]. Besides alloy composition, they vary with doping [40] and temperature, which might play a relevant role in this device, where the maximum internal temperature increase is of the order of 200 °C (at device turn-off). To better illustrate the influence of diffusion on mode competition, in Fig. 13 the modally resolved output powers are reported vs. current and compared to the experimental values.

These results are extracted from the optical spectra peaks and normalized for each current to provide the total measured power [30]. Varying the QW electron diffusion is dramatic; in particular, using the value as it stems from the Einstein relation with mobility, results in a delayed mode competition. In fact, the first-order mode power crosses that of the fundamental mode too late. Moreover, the third transverse mode just lases at the end of the operation, close to turn-off (15 mA), while experimentally it appears at about 8 mA, before power rollover. A similar behavior is reproduced by VENUS only by assuming a reduced electron diffusion by a factor of 2.5, which better fits the more important (because at the beginning of the laser action, in the linear VCSEL operation range) fundamental-to-first-order mode competition. Mobility reductions have already been discussed in the literature and can be ascribed to well-barrier interface roughness [56].

### F. Thermal conductivity thermal dependence

As anticipated previously, it is worth reporting in Fig. 14 on the overall performance impact of the thermal nonlinear coefficient ($\beta_T$ in (4)). The effect on both electrical and optical performance is somehow surprising. In fact, by directly acting on the temperature profile, it not only has an impact on the optical characteristics via the free-carrier absorption dependence and gain red-shift, but also on the electrical
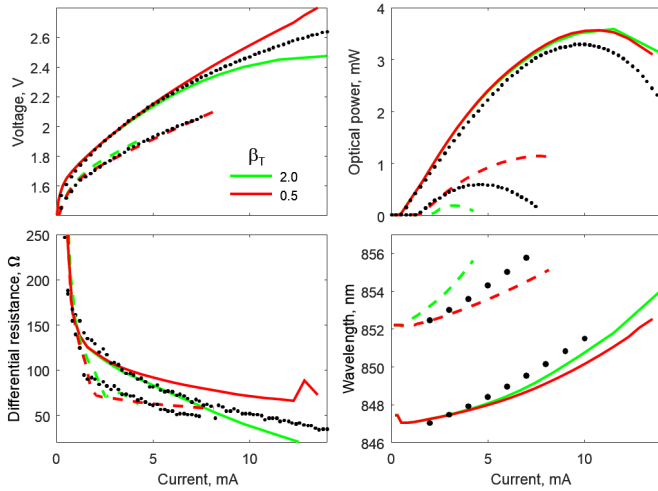
Fig. 14. VENUS output chart where the thermal conductivity exponent $\beta_T$ is varied around the typical values of 1.3 for the AlGaAs system.



Fig. 15. Longitudinal dependence of $n$-/$p$-currents around the MQW region at two injection levels (left, 2 mA; center, 15 mA, represented by the two green lines). Left, leakage current vs. injection current.

features. They depend weakly on temperature via the assumed thermal dependence of the mobility, but more strongly on the inherent dependences of the whole drift-diffusion problem on the temperature profile: Fermi functions and bandgaps. This result has to be compared with that of Fig. 7, which instead introduces just a scaling factor to the temperature, resulting in smaller variations of the electrical performance.

### G. Leakage currents

The roll-over and then the turn-off of a VCSEL has another subtle ingredient: current leakage [30], [57], [58]. In VENUS this effect is automatically included and it is worth to show how it contributes to the overall operation. To that end, in Fig. 15 the current leakage is reported, together with a detail of the $n$-/$p$- current longitudinal profiles (at each longitudinal section, the integral over the radial coordinates) around the active region at low and extreme operation conditions. From them, by the way, one can see that the sum of the $n$-,$p$-currents is constant and therefore the continuity of the current verified. The leakage current is extracted from the $n$-/$p$- currents at every computation step; there is zero leakage current when all the $p$- is converted into $n$-current within the MQW region. This roughly occurs at low injection (left), but thermal effects and band bending at high injection (central plot) causes a clear departure from this ideal condition.

## V. BROAD TEMPERATURE RANGE OPERATION PREDICTION

By adopting the parameter set of Table I, the overall result is presented Fig. 16. The full VENUS chart, including also non-observable quantities, reports the results at the four measured temperatures. Here (top center) also the central QW (and similar for the other QWs) $n$-/$p$-carrier densities on device axis are shown vs. current, but only for the two extreme temperatures, to avoid a too messy plot. In this plot we report the free (3D) carriers in the QW section, whose interactions with the confined (2D) ones are ruled by the capture model [59], [60]. It can be noticed that 3D carriers, especially electrons, increase
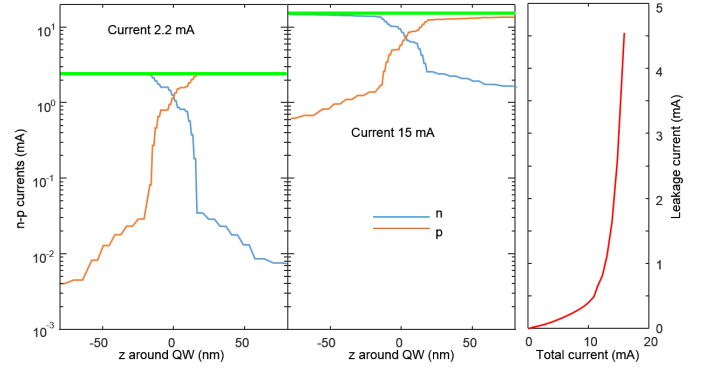
strongly after the rollover. These free carriers also contribute to the increase of the absorption losses via (7). Below the carrier plot, the maximum inner temperature increase is also shown up to VCSEL turnoff. From here it can be seen that the turnoff occurs roughly at the same total temperarure, once the increase is summed to the increased ambient temperature. The effect of the nonlinear termal coefficient can also be appreciated in this plot, even if the higher temperature slope is also due to the higher heat-sources related to the stronger recombinations

Both electrical and optical features can be reproduced satisfactorily. On the electrical side we observe that the *IV* curves match well, reproducing the voltage decrease at increasing temperature. The transition to conduction of the diode is better seen on the differerential resistance inset. As discussed before, this plot amplifies small numerical variations in the computed current, defined in VENUS as the integral of the current density at the ground contact. The important trends are all reproduced, *i.e.* the resistance decrease at increasing driving current and smaller values for higher temperatures.

On the optical side, threshold currents are fairly reproduced, thanks to the linear dependence of the free-carrier absorption on the ambient temperature. At the same time, this also provides not only a precise match of the optical slope ($dL/dI$), but also a fair estimate of the power rollover and even of the laser turn-off. To the best of our knowledge this is the first time that a multiphysics simulator is shown capable of tracking such extreme conditions. Previously, similar fits were applied in the framework of rate-equation approaches [61], [62], but with many more fit parameters and poorer comparison to experiments.

From this simulation campaign it comes clear that a VCSEL is a really complicated object, including phenomena not understood in full. This is especially true in extreme operation conditions, with some 200 K temperature increase compared to room temperature, where all the involved parameters are better known/investigated. Therefore we had to resort to the fitting procedure reported in this paper. It has to be underlined that our fitting procedure is rough, as also shown by the "round values" adopted. In fact, too much precision would be a nonsense, when we have at disposal many fitting parameters. One could think that other sets of parameters would provide similar
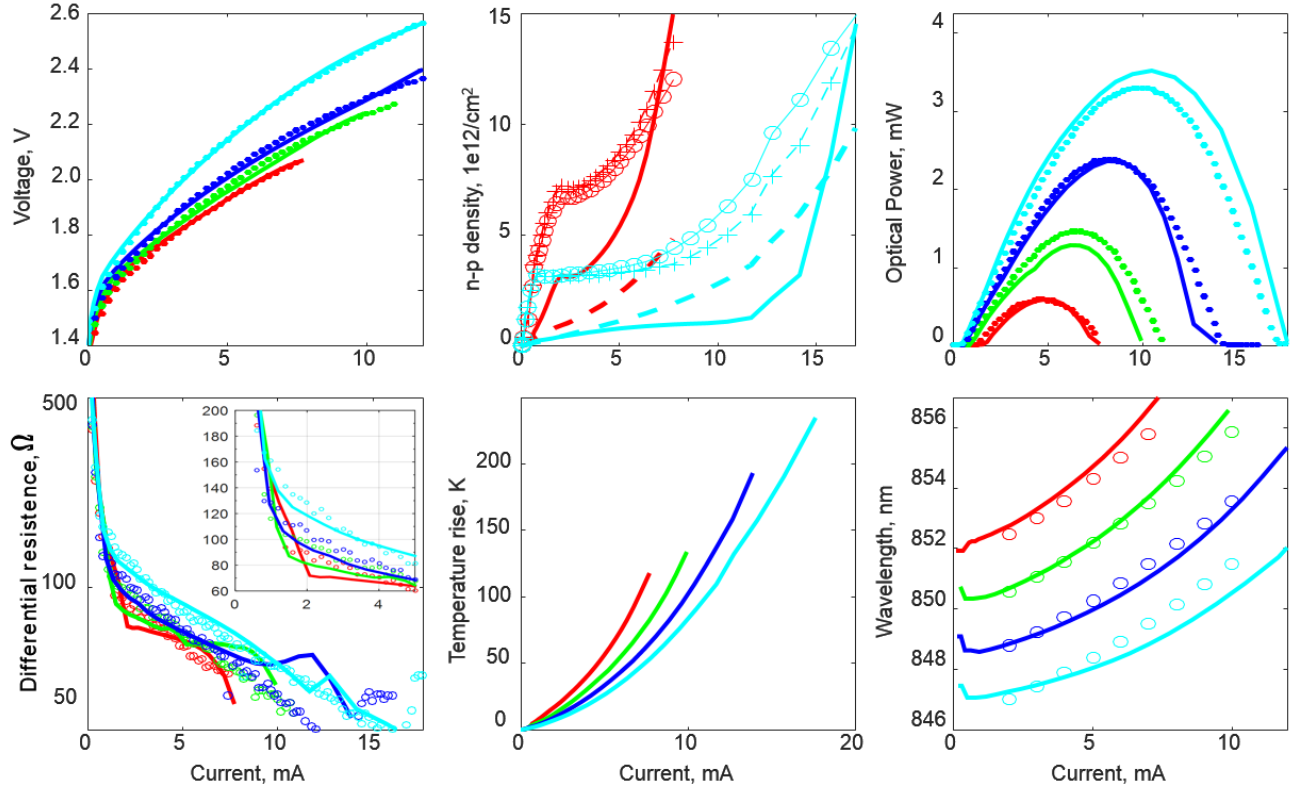
Fig. 16. VENUS full chart for the ambient temperatures set to 20, 50, 80, and 110 °C correspond to cyan, blue, green and red lines (VENUS) / symbols (experiments). For the parameters, refer to table I, for line meanings, see text. Differential resistance in logscale. In the central-top plot, the thick lines report the free (3D) electrons multiplied by the well thickness: continuous for electrons, dashed for holes. The lines with markers correspond to confined carriers: open circles for electrons, + for holes.

features. This is not the case, if not in a very minor sense; in fact, the fits were performed after identifying where each parameter has its main imparct and the other ones play minor roles.

In summary, we adopt the following fitting procedure. First, we consider the thermal problem, which influences all the others, and make sure that the thermal conductivity values and thermal dependence correctly fit the experiments (refer to end of Section II, Fig. 14 and Fig. 16).

Then the electrical characteristics are investigated and found to be mainly ruled by the carrier mobility. The available experimental data, previously measured in Ulm at room temperature, provide an important progress to the standard Hilsum formula, which overestimates the decrease of the mobility with the dopants. However, we still miss mobility temperature dependence. It is in our plans to repeat Hall measurements for different temperatures and extract such variations in the future. For the time being, we resorted to the fit proposed here, to mimic the improved electrical characteristics with temperature, using the exponential law in (6) just as a refinement.

In this paper we show, somehow unexpected, that the optical problem is governed by the FCA (free-carrier absorption); this is very clearly seen in Fig. 10. Apparently FCA is one of the most unknown ingredient in VCSEL simulation. In fact, the standard techniques used to compute this contribution provide much smaller values that the ones used in the literature [43, p. 175], which in this paper have been found to need a tem-

perature dependence too. It might be questioned whether there might be a problem in the parameters used in our gain model, which are however those reported in the literature. As said, a gain measurement campaign is need to double-check this point. For the time being, we resort to the phenomenological FCA proposed here.

The paper allows to better understand/quantify the thermal mechanisms that governs the VCSEL operation. As the internal temperature increases, which happens while increasing the current to get higher optical power, larger losses and lower gain result. The latter requires for higher carrier densities, and, overall, stronger heating sources, and therefore higher and higher temperatures, which lead, at the end, to the VCSEL turn-off.

The found parameters should be effective for a given technology, and so we expect they can be applied to other devices grown in Ulm. We will test this for the other oxide sizes available on our sample in the near future, and it would be even more useful to test another wafer design too. Finding such parameters for other technologies/labs, after acquiring this experience, would be quite simple and fast, thanks to all the optimizations introduced into VENUS. For this project, we explored up to 12 parameters at the two extreme temperatures. At 110 °C it took 16 hours, with an average of 80" per applied voltage on a not-to-date PC: Intel Core i7-4770 (3.4GHz) . Such simulation is run with just one main Matlab script, which is organized into nested parameter loops. The two temperature
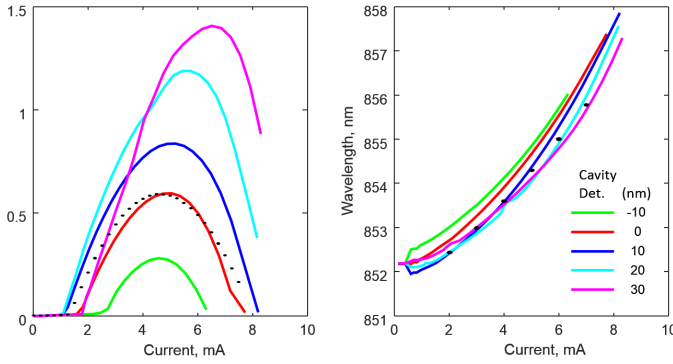
Fig. 17. Left: optical power vs. current for different gain-detuning values. Righ: the corresponding fundamental mode wavelengths. Results assume an ambient temperature of 130 °C; the experimental results at 110 °C are reported for reference.

sets are parallelized, so as to speed up the computation.

In Fig. 17, to give a flavor of VENUS potential, we investigate the ability of this device to work in extreme conditions, for *e.g.* datacenter racks. Therefore, aiming at improving high temperature performance, the VCSEL optical charateristics at 130 °C are computed for different gain-cavity detunings. This is performed in a somehow "fake" way; in fact, other then modifying the VCSEL layer thicknesses or QWs features, as it should be in a real device, we shift here the gain profile. The electrical characteristics are only affected in a minor way, and not shown here. It clearly appears that the actual structure was not designed for high temperature operation. In fact 0-detuning corresponds nearly to optimal performance at 20 °C, while at 130 °C, by applying a 20nm gain-shift, leads to a doubled output power and a reduced threshold. The effect of a higher output power can be seen also in the wavelength curves, where the lower heating due to the higher optical output, corresponds to a reduced red-shift.

## VI. CONCLUSIONS AND OUTLOOK

In conclusion, we have presented a detailed numerical investigation of thermal performance of an oxide-confined AlGaAs VCSEL, which has been experimentally characterized over a wide range of ambient temperatures. We determined a complete set of best-fit parameters, which allow to match the experimental results at all temperatures. As a consequence we are in a position to better qualify/quantify the reasons for power rollover and turn-off of the laser. We found that neither current leakage, nor Auger recombinations are sufficient, and that the major role is played by free-carrier absorption and their dependence on temperature. This phenomenon certainly deserves future efforts towards a rigorous modeling.

We plan to apply VENUS to different structures and material systems as soon as experimental data will be available. One future goal will concern similar experimental-numerical investigations of other important features, beyond steady state, such as small-signal modulation analysis and noise properties (RIN and linewidth).

## REFERENCES

[1] R. Michalzik, Ed., *VCSELs: Fundamentals, Technology and Applications of Vertical-Cavity Surface-Emitting Lasers*. Berlin: Springer-Verlag, 2013.

[2] H. Moench, M. Carpaij, P. Gerlach, S. Gronenborn, R. Gudde, J. Hellmig, J. Kolb, and A. v.d. Lee, "VCSEL based sensors for distance and velocity," in *Proc. SPIE 9766*, Mar. 2016, pp. 97 660A–1–16.

[3] K. J. Ebeling, R. Michalzik, and H. Moench, "Vertical-cavity surface-emitting laser technology applications with focus on sensors and three-dimensional imaging," *Japan. J. Appl. Phys.*, vol. 52, pp. 08PA02–1–11, 2018.

[4] M. Streiff, A. Witzig, M. Pfeiffer, P. Royo, and W. Fichtner, "A comprehensive VCSEL device simulator," *IEEE J. Select. Topics Quantum Electron.*, vol. 9, no. 3, pp. 879–891, 2003.

[5] K. Mehta, Y.-S. Liu, J. Wang, H. Jeong, T. Detchprohm, Y. J. Park, S. R. Alugubelli, S. Wang, F. A. Ponce, S.-C. Shen, R. D. Dupuis, and P. D. Yoder, "Lateral current spreading in III-N ultraviolet vertical-cavity surface-emitting lasers using modulation-doped short period superlattices," *IEEE J. Quantum Electron.*, vol. 54, no. 4, p. 2400507, Aug. 2018.

[6] *ISE TCAD Release 10.0*, Integrated Systems Engineering AG, Zurich, Switzerland, 2004.

[7] *Sentaurus Device User Guide. Version M-2017.09*, Synopsys, Inc., Mountain View, CA, Sept. 2017.

[8] *RSoft LaserMOD User Guide, v2018.03*, Synopsys, Inc., Optical Solutions Group, Ossining, NY, 2018.

[9] *Crosslight Device Simulation Software. General Manual*, Crosslight Software Inc., Vancouver, BC, Canada, Sept. 2014.

[10] A. Tibaldi, F. Bertazzi, M. Goano, R. Michalzik, and P. Debernardi, "VENUS: a Vertical-cavity surface-emitting laser Electro-opto-thermal NUmerical Simulator," *IEEE J. Select. Topics Quantum Electron.*, vol. 25, no. 6, pp. 1—1, 2019.

[11] P. Debernardi and R. Orta, "Analytical electromagnetic solution for Bragg mirrors with graded interfaces and guidelines for enhanced reflectivity," *IEEE J. Quantum Electron.*, vol. 43, no. 3, pp. 269–274, Mar. 2007.

[12] M. Daubenschüz and R. Michalzik, "Parameter extraction from temperature-dependent light-current-voltage data of vertical-cavity surface-emitting lasers," in *Proc. SPIE 9892*, Appl. Phys. Rev. 2016, pp. 98 920R–1–8.

[13] G. P. Bava, P. Debernardi, and L. Fratta, "Three-dimensional model for vectorial fields in vertical-cavity surface-emitting lasers," *Phys. Rev. A*, vol. 63, no. 2, pp. 23 816–1–23 816–13, 2001.

[14] P. Debernardi and G. P. Bava, "Coupled mode theory: a powerful tool for analyzing complex VCSELs and designing advanced devices features," *IEEE J. Select. Topics Quantum Electron.*, vol. 9, no. 3, pp. 905–917, 2003.

[15] P. Debernardi, J. M. Ostermann, M. Sondermann, T. Ackermann, G. P. Bava, and R. Michalzik, "Theoretical-experimental study of the vectorial modal properties of polarization-stable multimode grating VCSELs," *IEEE J. Select. Topics Quantum Electron.*, vol. 13, no. 5, pp. 1340–1348, 2007.

[16] K. Panajotov, B. Nagler, G. Verschaffelt, A. Georgievski, H. Thienpont, J. Danckaert, and I. Veretennicoff, "Impact of in-plane anisotropic strain on the polarization behavior of vertical-cavity surface-emitting lasers," *Appl. Phys. Lett.*, vol. 77, no. 11, pp. 1590–1592, 2000.

[17] P. Debernardi and G. P. Bava, "Effects of anisotropies on vectorial modes of vertical-cavity surface-emitting lasers," *Phys. Status Solidi A*, vol. 188, no. 3, pp. 967–977, 2001.

[18] T. Pusch, M. Lindemann, N. Gerhardt, M. Hofmann, and R. Michalzik, "Impact of in-plane anisotropic strain on the polarization behavior of vertical-cavity surface-emitting lasers," *Electron. Lett.*, vol. 51, no. 20, pp. 1600–1602, 2015.

[19] P. Debernardi, H. J. Unold, J. Maehnss, R. Michalzik, G. P. Bava, and K. J. Ebeling, "Single-mode, single-polarization VCSELs via elliptical surface etching: experiments and theory," *IEEE J. Select. Topics Quantum Electron.*, vol. 9, no. 5, pp. 1394–1405, 2003.

[20] J. M. Ostermann, P. Debernardi, C. Jalics, and R. Michalzik, "Polarization-stable oxide-confined VCSELs with enhanced single-mode output power via monolithically integrated inverted grating reliefs," *IEEE J. Select. Topics Quantum Electron.*, vol. 11, no. 5, pp. 982–989, 2005.

[21] P. Debernardi, R. Orta, T. Gründl, and M.-C. Amann, "3-D vectorial optical model for high-contrast grating vertical-cavity surface-emitting lasers," *IEEE J. Quantum Electron.*, vol. 49, no. 2, pp. 137–145, 2013.

[22] A. Tibaldi, P. Debernardi, and R. Orta, "High-contrast grating performance issues in tunable VCSELs," *IEEE J. Quantum Electron.*, vol. 51, no. 12, p. 2400407, 2015.

[23] R. Orta, A. Tibaldi, and P. Debernardi, "Bimodal resonance phenomena–part I: generalized Fabry–Pérot interferometers," *IEEE J. Quantum Electron.*, vol. 52, no. 12, pp. 6 100 508–1–8, 2016.

[24] A. Tibaldi, P. Debernardi, and R. Orta, "Bimodal resonance phenomena–part III: high-contrast grating reflectors," *IEEE J. Quantum Electron.*, vol. 54, no. 6, pp. 6 600 108–1–8, 2018.

[25] P. Debernardi, G. P. Bava, C. Degen, I. Fischer, and W. Elsäßer, "Influence of anisotropies on transverse modes in oxide-confined VCSELs," *IEEE J. Quantum Electron.*, vol. 38, no. 1, pp. 73–84, 2002.

[26] M. Farzaneh, R. Amatya, D. Lüerßen, K. J. Greenberg, W. E. Rockwell, and J. A. Hudgings, "Temperature profiling of VCSELs by thermoreflectance microscopy," *IEEE Photon. Technol. Lett.*, vol. 19, no. 8, pp. 601–603, 2007.

[27] S. Gehrsitz, F. K. Reinhart, C. Gourgon, N. Herres, A. Vonlanthen, and H. Sigg, "The refractive index of $Al_xGa_{1-x}As$ below the band gap: accurate determination and empirical modeling," *J. Appl. Phys.*, vol. 87, no. 13, pp. 7825–7837, 2000.

[28] J. S. Gustavsson, J. A. Vukusic, J. Bengtsson, and A. Larsson, "A comprehensive model for the modal dynamics of vertical-cavity surface-emitting lasers," *IEEE J. Quantum Electron.*, vol. 38, no. 2, pp. 203–212, 2002.

[29] M. Calciati, A. Tibaldi, F. Bertazzi, M. Goano, and P. Debernardi, "Many-valley electron transport in AlGaAs VCSELs," *Semiconductor Sci. Tech.*, vol. 32, no. 5, p. 055007, 2017.

[30] P. Debernardi, A. Kroner, F. Rinaldi, and R. Michalzik, "Surface relief versus standard VCSELs: a comparison between experimental and hot-cavity model results," *IEEE J. Select. Topics Quantum Electron.*, vol. 15, no. 3, pp. 828–837, 2009.

[31] M. A. Afromowitz, "Thermal conductivity of $Ga_{1-x}Al_xAs$ alloys," *J. Appl. Phys.*, vol. 44, no. 3, pp. 1292–1294, Mar. 1973.

[32] S. Mei and I. Knezevic, "Thermal conductivity of III-V semiconductor superlattices," *J. Appl. Phys.*, vol. 118, pp. 175 101–1–8, 2015.

[33] Y. Huo, C. Y. Cho, K. F. Huang, Y. F. Chen, and C. C. Lee, "Exploring the DBR superlattice effect on the thermal performance of a VECSEL with the finite element method," *Opt. Lett.*, vol. 44, no. 2, pp. 327–330, 2019.

[34] C. Canuto, M. Y. Hussaini, A. Quarteroni, and T. A. Zang, *Spectral methods: evolution to complex geometries and applications to fluid dynamics*, 1st ed. Berlin: Springer-Verlag, 2007.

[35] A. Tibaldi, R. Orta, O. A. Peverini, G. Addamo, G. Virone, and R. Tascone, "Skew incidence plane-wave scattering from 2-D dielectric periodic structures: analysis by the mortar-element method," *IEEE Trans. Microwave Theory Tech.*, vol. 63, no. 1, pp. 11–19, 2015.

[36] A. Tibaldi, "A mortar element method for the analysis of electromagnetic passive devices," Ph.D. dissertation, Politecnico di Torino, Jan. 2016.

[37] D. Gottlieb and S. A. Orszag, *Numerical analysis of spectral methods: theory and applications*, 1st ed. Philadelphia: SIAM, 1977.

[38] S. Adachi, Ed., *Properties of Aluminium Gallium Arsenide*, ser. EMIS Datareviews Series. London: INSPEC, 1993.

[39] Y. P. Varshni, "Temperature dependence of the energy gap in semiconductors," *Physica*, vol. 34, no. 1, pp. 149–154, 1967.

[40] C. Hilsum, "Simple empirical relationship between mobility and carrier concentration," *Electron. Lett.*, vol. 10, no. 13, pp. 259–260, 1974.

[41] S. Zollner, P. P. Paradis, F. Abadizaman, and N. S. Samarasingha, "Drude and Kukharskii mobility of doped semiconductors extracted from Fourier-transform infrared ellipsometry spectra," *J. Vac. Sci. Technol. B*, vol. 37, no. 1, p. 012904, 2019.

[42] E. Haga and H. Kimura, "Free-carrier infrared absorption in III-V semiconductors III. GaAs, InP, GaP and GaSb," *J. Phys. Soc. Japan*, vol. 19, no. 5, pp. 658–669, 1964.

[43] H. C. Casey, Jr. and M. B. Panish, *Heterostructure Lasers. Part A: Fundamental Principles*. New York: Academic Press, 1978.

[44] S. L. Chuang, *Physics of Photonic Devices*. Hoboken: John Wiley & Sons, 2009.

[45] R. W. Martin and H. L. Störmer, "On the low energy tail of the electron-hole drop recombination spectrum," *Solid State Commun.*, vol. 22, pp. 523–526, 1977.

[46] A. Tomita and A. Suzuki, "A new density matrix theory for semiconductor lasers, including non-Markovian intraband relaxation and its application to nonlinear gain," *IEEE J. Quantum Electron.*, vol. 27, no. 6, pp. 1630–1641, 1991.

[47] F. Bertazzi, M. Goano, G. Ghione, A. Tibaldi, P. Debernardi, and E. Bellotti, "Electron transport," in *Handbook of Optoelectronic Device Modeling and Simulation*, J. Piprek, Ed. Boca Raton, FL: CRC Press, 2017, ch. 2, pp. 35–80.

[48] F. Bertazzi, M. Goano, and E. Bellotti, "Calculation of Auger lifetime in HgCdTe," *J. Electron. Mater.*, vol. 40, no. 8, pp. 1663–1667, 2011.

[49] M. Calciati, M. Goano, F. Bertazzi, M. Vallone, X. Zhou, G. Ghione, M. Meneghini, G. Meneghesso, E. Zanoni, E. Bellotti, G. Verzellesi, D. Zhu, and C. Humphreys, "Correlating electroluminescence characterization and physics-based models of InGaN/GaN LEDs: Pitfalls and open issues," *AIP Adv.*, vol. 4, no. 6, p. 067118, June 2014.

[50] F. Bertazzi, M. Goano, X. Zhou, M. Calciati, G. Ghione, M. Matsubara, and E. Bellotti, "Looking for Auger signatures in III-nitride light emitters: A full-band Monte Carlo perspective," *Appl. Phys. Lett.*, vol. 106, no. 6, p. 061112, Feb. 2015.

[51] J. Piprek, "What limits the efficiency of high-power InGaN/GaN lasers?" *IEEE J. Quantum Electron.*, vol. 53, no. 1, pp. 1–4, Feb. 2017.

[52] J. Piprek, F. Römer, and B. Witzigmann, "On the uncertainty of the Auger recombination coefficient extracted from InGaN/GaN light-emitting diode efficiency droop measurements," *Appl. Phys. Lett.*, vol. 106, no. 10, p. 101101, 2015.

[53] U. Strauss, W. W. Rühle, and K. Köhler, "Auger recombination in intrinsic GaAs," *Appl. Phys. Lett.*, vol. 62, no. 1, pp. 55–57, Jan. 1993.

[54] M. Takeshima, "Effect of Auger recombination on laser operation in $Ga_{1-x}Al_xAs$," *J. Appl. Phys.*, vol. 58, no. 1, pp. 3846–3850, Nov. 1985.

[55] "Physical properties of semiconductors," Ioffe Physico-Technical Institute, St. Petersburg, Russia. [Online]. Available: http://www.ioffe.ru/SVA/NSM/Semicond/index.html

[56] H. Sakaki, T. Noda, K. Hirakawa, M. Tanaka, and T. Matsusue, "Interface roughness scattering in GaAs/AlAs quantum wells," *Appl. Phys. Lett.*, vol. 51, no. 23, pp. 1934–1936, 1987.

[57] G. R. Hadley, K. L. Lear, M. E. Warren, K. D. Choquette, J. W. Scott, and S. W. Corzine, "Comprehensive numerical modeling of vertical-cavity surface-emitting lasers," *IEEE J. Quantum Electron.*, vol. 32, no. 4, pp. 607–616, 1996.

[58] P. Debernardi, "HOT-VELM: a comprehensive and efficient code for fully vectorial and 3-D hot-cavity VCSEL simulation," *IEEE J. Quantum Electron.*, vol. 45, no. 8, pp. 979–992, 2009.

[59] M. Goano, F. Bertazzi, X. Zhou, M. Mandurrino, S. Dominici, M. Vallone, G. Ghione, A. Tibaldi, M. Calciati, P. Debernardi, F. Dolcini, F. Rossi, G. Verzellesi, M. Meneghini, N. Trivellin, C. De Santi, E. Zanoni, and E. Bellotti, "Challenges towards the simulation of GaN-based LEDs beyond the semiclassical framework," in *SPIE Photonics West, Physics and Simulation of Optoelectronic Devices XXIV*, B. Witzigmann, M. Osiński, and Y. Arakawa, Eds., vol. 9742, Proceedings of the SPIE, San Francisco, CA, Feb. 2016, p. 974202.

[60] C. De Santi, M. Meneghini, A. Tibaldi, M. Vallone, M. Goano, F. Bertazzi, G. Verzellesi, G. Meneghesso, and E. Zanoni, "Physical mechanisms limiting the performance and the reliability of GaN-based LEDs," in *Nitride Semiconductor Light-Emitting Diodes*, 2nd ed., J. J. Huang, H. C. Kuo, and S.-C. Shen, Eds. Duxford, U.K.: Woodhead Publishing, 2018, ch. 14, pp. 455–489.

[61] W. Nakwaski and M. Osinski, "Thermal properties of etched-well surface-emitting semiconductor lasers," *IEEE J. Quantum Electron.*, vol. 27, no. 6, pp. 1391–1401, 1991.

[62] J. W. Scott, R. S. Geels, S. W. Corzine, and L. A. Coldren, "Modeling temperature effects and spatial hole burning to optimize vertical-cavity surface-emitting laser performance," *IEEE J. Quantum Electron.*, vol. 29, no. 5, pp. 1295–1308, 1993.

**Pierluigi Debernardi** was born in Casale Monferrato and received his degree in Electronics Engineering in 1987 from Politecnico di Torino, Italy. Since 1989 he's with the Italian National Council of Research at Politecnico di Torino. His interests are mainly in the field of the modeling of semiconductor materials and devices for optoelectronic applications. Recently he is mostly involved in modeling and designing VCSEL structures with non-circular and/or complex geometries, so as to achieve specific performances.
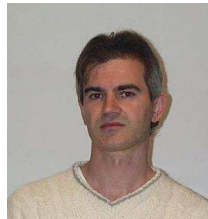
**Michele Goano** (M'98) received the Laurea and Ph.D. degrees in electronic engineering from Politecnico di Torino, Turin, Italy, in 1989 and 1993, respectively. In 1994 and 1994, he was a Post-Doctoral Fellow with the Département de Génie Physique, École Polytechnique de Montréal, Montréal, QC, Canada. He joined the faculty of Politecnico di Torino in 1995. He has been a visiting scholar with the School of Electrical and Computer Engineering, Georgia Institute of Technology, Atlanta, GA, USA, with the Department of Information Technology and Media, Mid-Sweden University, Sundsvall, Sweden, and with the Department of Electrical and Computer Engineering, Boston University, Boston, MA, USA. His current research activity is focused on the simulation of optoelectronic devices based on narrow- and wide-bandgap semiconductor materials.

**Alberto Tibaldi** was born in Casale Monferrato, Italy, in 1987. In 2009, 2011 and 2015 he received the B.Sc., M.Sc. and Ph.D. degrees in Electronic Engineering from Politecnico di Torino. In 2012 he joins the Italian National Council of Research (CNR) as a research fellow. Currently he teaches courses on numerical analysis and semiconductor device simulation. His scientific interests mainly regard the electrical and optical modeling of photonic devices.

**Markus Daubenschüz** received his B.Sc. and his M.Sc. in Electronical Engineering of the FernUniversität Hagen, Germany in 2007 and 2012, respectively. From 2013 until 2017 he was a research stuff member in the VCSELs and Optical Interconnects research group at Ulm University, Germany. His scientific interest is mainly on device simulation and characterization. Since 2017 he is working as a VCSEL design engineer at Philips Photonics in Ulm, Germany.

**Francesco Bertazzi** received the Laurea and Ph.D. degrees in electronics engineering from Politecnico di Torino, Turin, Italy, in 2000 and 2003, respectively. He was a Visiting Scholar with the Department of Electrical and Computer Engineering at Boston University, Boston, MA. Since 2008 he is professor at the Dipartimento di Elettronica, Politecnico di Torino. His research activities include material-theory-based modeling of band structures, vibrational properties, full-band Monte Carlo and nonequilibrium Green's function modeling of carrier transport in optoelectronic devices (HgCdTe infrared photodetectors, InGaN light-emitting diodes and VCSELs).

**Rainer Michalzik** received the Dipl.-Ing. degree in electrical engineering from the Technical University of Braunschweig, Braunschweig, Germany, in 1989, and the Dr.-Ing. and habilitation degrees from Ulm University, Ulm, Germany, in 1996 and 2009, respectively. He was appointed as an apl. Prof. in 2012.
Since 2001 he has been leading the VCSELs and Optical Interconnects Research Group, Institute of Functional Nanosystems (Inst. of Optoelectronics until June 30, 2018), Ulm University, Ulm, Germany. He has edited the book entitled *VCSELs — Fundamentals, Technology and Applications of Vertical-Cavity Surface-Emitting Lasers* (Berlin, Germany: Springer, 2013).